Chem Catalysis

CellPress

Article

Fe on molecular-layer MoS_2 as inorganic Fe-S_2-Mo motifs for light-driven nitrogen fixation to ammonia at elevated temperatures

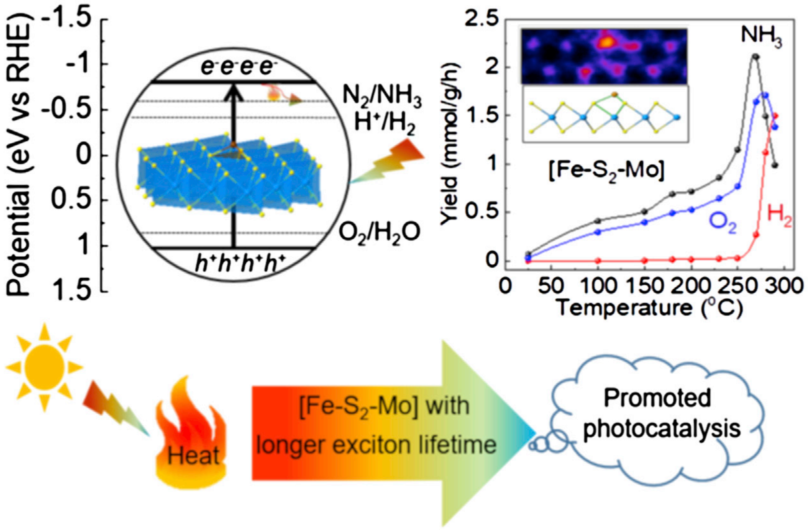

An inorganic catalyst with [Fe-S_2-Mo] motifs with a connecting structure similar to that of FeMoco has been established for N_2 fixation at elevated temperature. The elevation of reaction temperature and adsorption of N_2 cause a significant suppression of electron-hole pair recombination and thus prolong the exciton lifetime for efficient ammonia synthesis. This method of ammonia production and these photocatalytic materials may open up an exciting possibility for the decentralization of ammonia production for fertilizer provision to local farmlands using solar illumination.

Jianwei Zheng, Lilin Lu,
Konstantin Lebedev, ...,
Yun-Liang Soo, Kazu Suenaga,
Shik Chi Edman Tsang

edman.tsang@chem.ox.ac.uk

Highlights

Fe-decorated 2D MoS_2 photocatalysts [Fe-S_2-Mo] were developed for N_2 fixation

Fe-S_2-Mo offered superior high activity and selectivity for NH_3 synthesis at 270°C

A solar-to-NH_3 energy-conversion efficiency of 0.24% was achieved at 270°C

Heating enhanced NH_3 production by suppressing electron-hole pair recombination in MoS_2

Zheng et al., Chem Catalysis *1*, 162–182
June 17, 2021 © 2021 Elsevier Inc.
https://doi.org/10.1016/j.checat.2021.03.002

CellPress

Chem Catalysis

Article

Fe on molecular-layer MoS_2 as inorganic Fe-S_2-Mo motifs for light-driven nitrogen fixation to ammonia at elevated temperatures

Jianwei Zheng,[1] Lilin Lu,[1,2] Konstantin Lebedev,[1] Simson Wu,[1] Pu Zhao,[1] Ian J. McPherson,[1] Tai-Sing Wu,[3] Ryuichi Kato,[4] Yiyang Li,[1] Ping-Luen Ho,[1] Guangchao Li,[1] Linlu Bai,[6] Jianhui Sun,[6] Dharmalingam Prabhakaran,[5] Robert A. Taylor,[5] Yun-Liang Soo,[3] Kazu Suenaga,[4] and Shik Chi Edman Tsang[1,7,*]

SUMMARY

Current industrial production of ammonia from the Haber-Bosch process and its transport concomitantly produces a large quantity of CO_2. Herein, we successfully synthesize inorganic-structure-based catalysts with [Fe-S_2-Mo] motifs with a connecting structure similar to that of FeMoco (a cofactor of nitrogenase) by placing iron atoms on a single molecular layer of MoS_2 at various loadings. This type of new catalytic material functionally mimics the nitrogenase to convert N_2 to ammonia and hydrogen in water without adding any sacrificial agent under visible-light illumination. Using the elevated temperature boosts the ammonia yield and the energy efficiency by one order of magnitude. The solar-to-NH_3 energy-conversion efficiency can be up to 0.24% at 270°C, which is the highest efficiency among all reported photocatalytic systems. This method of ammonia production and the photocatalytic materials may open up an exciting possibility for the decentralization of ammonia production for fertilizer provision to local farmlands using solar illumination.

INTRODUCTION

In nature, atmospheric nitrogen is biologically fixed into ammonia by nitrogenase enzymes (biological nitrogen fixation [BNF] process) in an associative manner under ambient conditions. As one of the most important artificial nitrogen fixations (ANF) discovered in the last century, the Haber-Bosch (HB) process immensely promotes food production.[1,2] However, this process is energy and carbon intensive as a result of multiple steps including the production of H_2 from methane reformation, air separation, and dissociative activation of N_2 at high temperature over metallic structures. Approximately 1.5 kg of CO_2 per kg of NH_3 is released to the atmosphere, which represents 0.93% of global greenhouse gas (GHG)[3] emissions. Recently, demonstration units for an electric HB process using renewable wind energy have been developed, and these generate H_2 from H_2O electrolysis for ammonia synthesis.[4,5]

In comparison, BNF with engineered enzymes at small scale may be able to produce ammonia. However, this still requires a large input of chemical energy provided by the hydrolysis of adenosine 5′-triphosphate (ATP).[6] Alternatively, using renewable electricity or light as the energy input instead of ATP over catalytic materials is a viable way to produce ammonia under ambient conditions. Yet the present rate of

The bigger picture

The decentralization of ammonia production for fertilizer to local farmlands using solar illumination is an attractive proposal for the future. Yet, the photocatalytic performance remains low, and a suitable setup has yet to be established as a result of the insufficient ability of catalysts to split the N≡N bond. In this work, inorganic-based catalysts with [Fe-S_2-Mo] motifs mimic FeMoco in nature for ammonia synthesis. Superior photocatalytic N_2 reduction is achieved with a solar-to-NH_3 energy-conversion efficiency of 0.24% at 270°C, which is the highest efficiency among all reported photocatalytic systems. Heat boosts the photocatalytic performance by suppressing the electron-hole pair recombination and thus prolongs the exciton lifetime for efficient ammonia synthesis. The heat can be derived from the solar absorption, thus providing an exciting possibility for the decentralization of ammonia production for fertilizer provision to local farmlands.

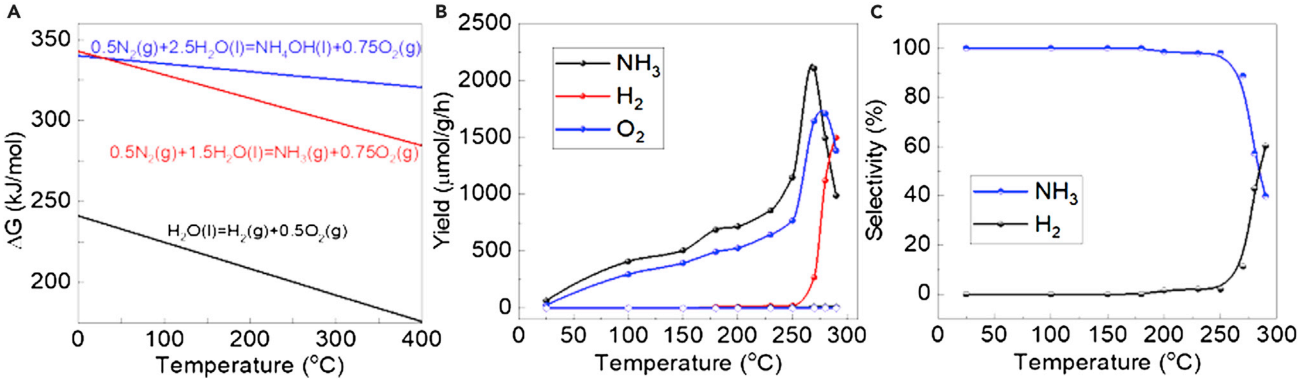

Figure 1. Thermodynamic and kinetic analyses of NH_3 synthesis and water splitting over Fe-sMoS$_2$ (3 wt %)

(A) Temperature dependences of the changes in the Gibbs free energy (ΔG) of NH_3 synthesis and water splitting.

(B) Production rates of NH_3, H_2, and O_2 as a function of temperature over Fe-sMoS$_2$. Results of controlled experiments under dark conditions are shown as empty symbols.

(C) Product selectivity of NH_3, H_2, and O_2 as a function of temperature over Fe-sMoS$_2$. A UV-cut tungsten light source and 6 bar of N_2 in water were used.

photo- or electrochemical ammonia synthesis over most reported heterogeneous materials is fairly low.

Iron (or sometimes molybdenum [Mo]) sulfur (Fe-S) clusters with tetrahedral Fe/Mo and weak field S ligands are the molecular electron relay centers for fast redox catalysis in biology.[7] In particular, nitrogenase is a multiprotein complex consisting of an Fe-S protein and an associated MoFe-S cluster protein (Figure S1). ATP is consumed at the Fe-S [4Fe-4S] protein, which also delivers the generated electrons by a remote outer-sphere mechanism[8] to the catalytic MoFe protein with the more extensive Fe-Mo cofactor (FeMoco) containing [Mo:7Fe:9S:C].[9] The electrons, once transferred, are believed to finally accumulate at the FeMoco via the essential electron relay of Fe-S cluster centers and can subsequently be used for the reduction of N_2.[10–12] The structural and functional mimic of nitrogenase to produce ammonia is a current endeavor in research but mainly through enzymatic processes.[13–15]

Here, we report that an inorganic-matter-based structure with [Fe-S_2-Mo] motifs (surface clusters including Fe, Fe_2S_2, Fe_3S_4, F_4S_4, and so on) with Fe atoms placed on a molecular layer of MoS_2 (Figure S1) at different loadings shows exceptional activity and efficiency for the conversion of N_2 to ammonia in water under visible-light illumination. Additional appropriate methodology of employing elevated temperatures improves the photocatalytic ammonia synthesis and energy efficiency. Detailed investigations indicate that elevated temperatures and the adsorption of N_2 prolong the exciton lifetime and suppress the electron-hole pair recombination in MoS_2, allowing the prior transfer of a photoelectron to nitrogen rather than to hydrogen, and thus significantly improving the overall ammonia synthesis when compared with the photolysis of water. Furthermore, a solar furnace was employed to mimic the solar light concentrator without any direct thermal energy to demonstrate the facile application for the decentralization of ammonia supply to local farmland.

RESULTS AND DISCUSSION

Thermodynamic and kinetic study of photocatalytic ammonia synthesis and water splitting

We estimated changes in Gibbs free energy by fixing the amounts of reactants. As shown in Figure 1A, both the nitrogen reduction to ammonia and water splitting to H_2 are difficult thermodynamically because of the large change in Gibbs free energy

[1]Wolfson Catalysis Centre, Department of Chemistry, University of Oxford, Oxford OX1 3QR, UK

[2]State Key Laboratory of Refractories and Metallurgy, Wuhan University of Science and Technology, China

[3]Department of Physics, National Tsing Hua University, Hsinchu, Taiwan

[4]National Institute of Advanced Industrial Science and Technology, Higashi, Tsukuba, Ibaraki 305-8565, Japan

[5]Clarendon Laboratory, Department of Physics, University of Oxford, Oxford OX1 3PU, UK

[6]Key Laboratory of Functional Inorganic Material Chemistry, Heilongjiang University, Ministry of Education, School of Chemistry and Materials Science, International Joint Research Center for Catalytic Technology, Harbin 150080 China

[7]Lead contact

*Correspondence: edman.tsang@chem.ox.ac.uk

https://doi.org/10.1016/j.checat.2021.03.002

(ΔG). Although increasing the reaction temperature facilitates the thermodynamics, the values are still more than 150 kJ mol^{-1}. Note that water splitting is more facile throughout the temperature range from 0°C to 400°C. However, a large number of photocatalytic results demonstrated that it is quite difficult to achieve water splitting without sacrificial agents at ambient conditions even under light illumination.[16,17] In our case, we can hardly detect any H_2 production except with a measurable amount of NH_3 over our 2D single-layered MoS_2 ($sMoS_2$) with [Fe-S_2-Mo] (hereafter referred to as Fe-$sMoS_2$) until the reaction temperature is above 180°C under visible-light illumination (Figure 1B). This shows that the ammonia yield is dependent on the reaction temperature maximum with a record yield of 2.1 mmol g^{-1} h^{-1} at 270°C (Table S1). However, as shown in Figure 1C, the selectivity of ammonia dramatically falls when the temperature is higher than 250°C, and more hydrogen is produced than NH_3 when the temperature is above 270°C (following the stoichiometric mole ratios in the reaction of $3{*}M(NH_3) + 2{*}M(H_2) = 4{*}M(O_2)$). The lower ammonia yield may be due to the competitive hydrogen production from water splitting. These results show that Fe-$sMoS_2$ can be used for ammonia synthesis and is kinetically more favorable than hydrogen evolution when the temperature is below 270°C. The catalyst has been recycled six times and run for 30 h without significant attenuation of ammonia yield (Figures S2 and S3), demonstrating that the Fe-$sMoS_2$ is stable despite the high temperature of 270°C used. It is well known that the ionization constant progressively increases and reaches the optimal value at 270°C.[18] In this current system, the total calculated yield of H-derived ammonia and H_2 also reaches the optimal value at 270°C. However, it is apparent that the hydrogen evolution reaction (HER) becomes more dominant than ammonia production when the temperature is greater than 250°C, offering progressively lower ammonia selectivity beyond this temperature. Given that N_2 reduction is expected to take place at the conduction band (CB) while the water oxidation occurs at the valence band (VB) during the light excitation, the rate of ammonia synthesis is at best equal to oxygen production but becomes slower at higher temperature. This is because of the competition for electrons between N_2 reduction and H_2 formation with protons. It is therefore important to suppress the HER reaction, which is competitive with the nitrogen reduction reaction at elevated temperatures. Blank experiments show that light illumination is essential for the photocatalytic ammonia synthesis (Figures 1B and S3B).

The quantum efficiency (QE) for photon-to-ammonia conversion is the key parameter in evaluating the efficiency of renewable-light energy conversion.[17] Figure S4 shows that the QE of this nitrogenase-mimic Fe-$sMoS_2$ can be up to 37.1% for ammonia synthesis at 432 nm, a value ten times that at room temperature. Although increasing the wavelength of monochrome light to 575 nm reduces the QE to 19.6%, this is still the highest value reported in photoammonia synthesis so far. Several studies also have comparable QE for hydrogen evolution from water at high reaction temperature, but the underlying reason for this remains unclear.[18] Isotope-labeled $^{15}N_2$ was used to track the nitrogen source of ammonia, which confirmed that gaseous $^{15}N_2$ in the sealed system was fixed by this FeMoco-like Fe-$sMoS_2$ (Figures S5 and S6). Ammonia measurement by the NMR method (Figure S7) is also agreeable with the result obtained from the ammonia electrode method (Figure S8) (for details, see Note S1). In addition, the ratio of H derived from NH_3 and H_2 and O from O_2 in the product as a function of reaction temperature is about 2 (Figures S9 and S10), further demonstrating the ammonia production from N_2 and water.

Structure of Fe-$sMoS_2$

The 2D single-molecular-layer MoS_2, consisting of three sublayers of S-Mo-S in a trigonal prismatic 2-H structure, was first synthesized via the well-established chemical exfoliation method by *n*-butyllithium.[19] Subsequently, Fe atoms were attached to $sMoS_2$ by a hydrothermal method for *in-situ*-formed sulfide species (Figures S11 and S12), followed by H_2 reduction to produce the molecular Fe-$sMoS_2$ in nanosize. In this synthesis, Fe atoms were well dispersed and assembled onto the basal plane of the $sMoS_2$. Similar transition-metal-doped catalysts were prepared in the same manner. No peaks corresponding to Fe-based aggregate species were detected in any of the X-ray diffraction (XRD) patterns (Figure S13), demonstrating the high dispersity of the Fe atom. The characteristic peaks of MoS_2 particularly stacking in the z axis with 2θ near 15° were diminished, indicating the thin layers of MoS_2 in Fe-$sMoS_2$ even after reduction. As shown by scanning transmission electron microscopy (STEM) in Figure S14, the dried sample contains many thin layers of MoS_2 with dispersed Fe_1 atoms. Some of these Fe atoms can be grouped into Fe_2, Fe_3, or Fe_4 S clusters at increasing loadings. Interestingly, the MoS_2 layers are assembled not in the original ordered layered structure but as random stacked multilayers.[20] The as-observed amorphous restacking indicates that they were initially separated into single layers before drying.

To investigate the aggregation, we performed X-ray pair distribution function (XPDF) because this technique takes both Bragg and diffuse components of the coherent scattering data into account to yield the structure parameters reflecting both the local structural disorder in materials and the long-range order. $sMoS_2$ and Fe-$sMoS_2$ showed attenuating XPDF signals from 7 to 20 Å (Figure S15), whereas in the longer range larger than 20 Å, the signal significantly decayed to 0, indicating that the as-reduced (dried) sample was indeed varied from one to three layers, as shown by the atomic force microscopy (AFM) data. Of particular interest, the signals at 7.11 and 7.78 Å corresponding to the Mo–Mo bond and Mo–S bond in two layers of MoS_2 in a crystalline form (Figure S15C) disappeared in the dried sample. This clearly indicates that MoS_2 was actually exfoliated into single layers (catalytic testing was carried out in solution) but restacked to two to three layers in a highly disordered manner after being dried (examined by AFM in Figure S12), so these two signals from the ordered layers vanished. Note that the random restacked one to two layers in dried form can be redispersed in solution to regenerate the single-layer materials.

Figure 2A shows a typical high-angle annular dark-field (HAADF)-STEM image of Fe-$sMoS_2$ (3 wt % Fe loading) with a corresponding 2-H characteristic pattern. The distinctive brighter spots above the surrounding Mo and S_2 sites in a 2-H arrangement in Figure 2A (white circles) and the enlarged image in Figure 2B show that individual Fe atoms are uniformly dispersed and overlap the position of Mo and S sites in the structural motif of 2H-$sMoS_2$. The edge of the single-layer material was unavoidably destroyed due to the strong electron beams. However, we did not see significant metal-containing aggregates at this loading; we did see dispersive single Fe atoms on $sMoS_2$, showing a higher adsorption energy on this S surface than for cohesive interactions.[19] To further confirm the nature of this adsorbed metal atom, we performed atomic-resolved electron energy-loss spectroscopy (EELS) on these brighter spots. The EELS (Figure 2C) at the corresponding positions demonstrates the presence of Fe atoms with the characteristic signature L_3 edge at 708 eV.[21] The images for HAADF-STEM and EELS analysis show that isolated Fe atoms are deposited at the two favored positions in the basal plane of $sMoS_2$. A typical intensity profile analysis of the HAADF image (Figure 2D) demonstrates that an Fe atom commonly takes residence on the atop site of Mo of the basal plane (blue and green lines). Occasionally, an Fe atom can be found in the position of a S site as a substitution (red line). The structural models shown in Figures 2E and 2F based

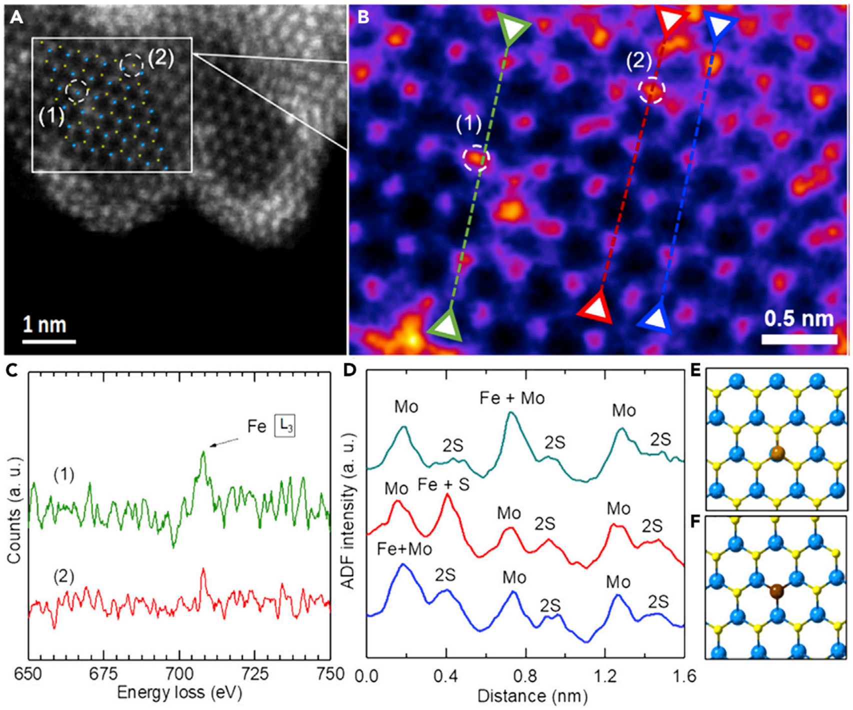

Figure 2. Characterization of the basal plane of Fe-sMoS$_2$ and identification of the Fe atoms

(A) HAADF-STEM image of the Fe-sMoS$_2$ (3 wt %).

(B) Atomic-resolution HAADF-STEM image of the basal plane of Fe-sMoS$_2$. Scan 1 (green line) contains an Fe atom on a Mo atop site, scan 2 (red line) contains a S vacancy substituted by an Fe atom, and the additional scan indicated by the blue line also shows an Fe atom on a Mo atop site.

(C) Atomic EELS acquired for spots 1 and 2 in (A): an EEL edge at 708 eV corresponds to the L$_3$ edge of the Fe atom.

(D) ADF intensity line profiles taken along the correspondingly numbered lines 1 and 2, indicated in (B).

(E) Atomic model based on optimized DFT for a single Fe atom on a Mo atop site.

(F) Atomic model based on optimized DFT for a single Fe atom substituting a S site. Blue and yellow balls represent Mo and S atoms, respectively.

on density functional theory (DFT) calculations also confirm the existence of these two energetically favored atomic positions (Figure S16).

As shown in k^3-weighted extended X-ray absorption fine structure (EXAFS) for Fe post-*k*-edge analysis of Fe-sMoS$_2$ (Figure 3A) with the low loading of 3 wt % Fe, there are clearly Fe–S contributions at a distance of 1.7 Å for Fe-sMoS$_2$, which is distinctively different from the Fe–Fe contributions (not detected) at a distance of 2.2 Å calibrated by an Fe foil. The curve fit matches the expected coordination number of the nearest S atoms around the isolated Fe atom of 2.7 with the distance of 2.1 Å according to the atop model (Figure S17 and Table S2). Figure 3B shows the wavelet transform (WT)-EXAFS analysis based on Morlet wavelets, which can be used to differentiate closely related spatial interactions.[22] For Fe-sMoS$_2$, the hot spot of the WT maximum at ~6 Å^{-1} is well resolved at the first coordination shell, which can clearly be related to the Fe–S bond at the atop site. In contrast, the WT intensity hot spot at ~8 Å^{-1} corresponding to the Fe–Fe bond was not detected in Fe-sMoS$_2$ (Figure S18), indicating that the Fe single atom is a dominant feature. Notably, there is no clear WT intensity for Fe at the S substitution site, demonstrating that this is the principal site for Fe. In addition, we simulated the structures for Fe on the atop Mo site of MoS$_2$ and Fe-substituted Mo site of MoS$_2$ (top and bottom in Figure 3D) and

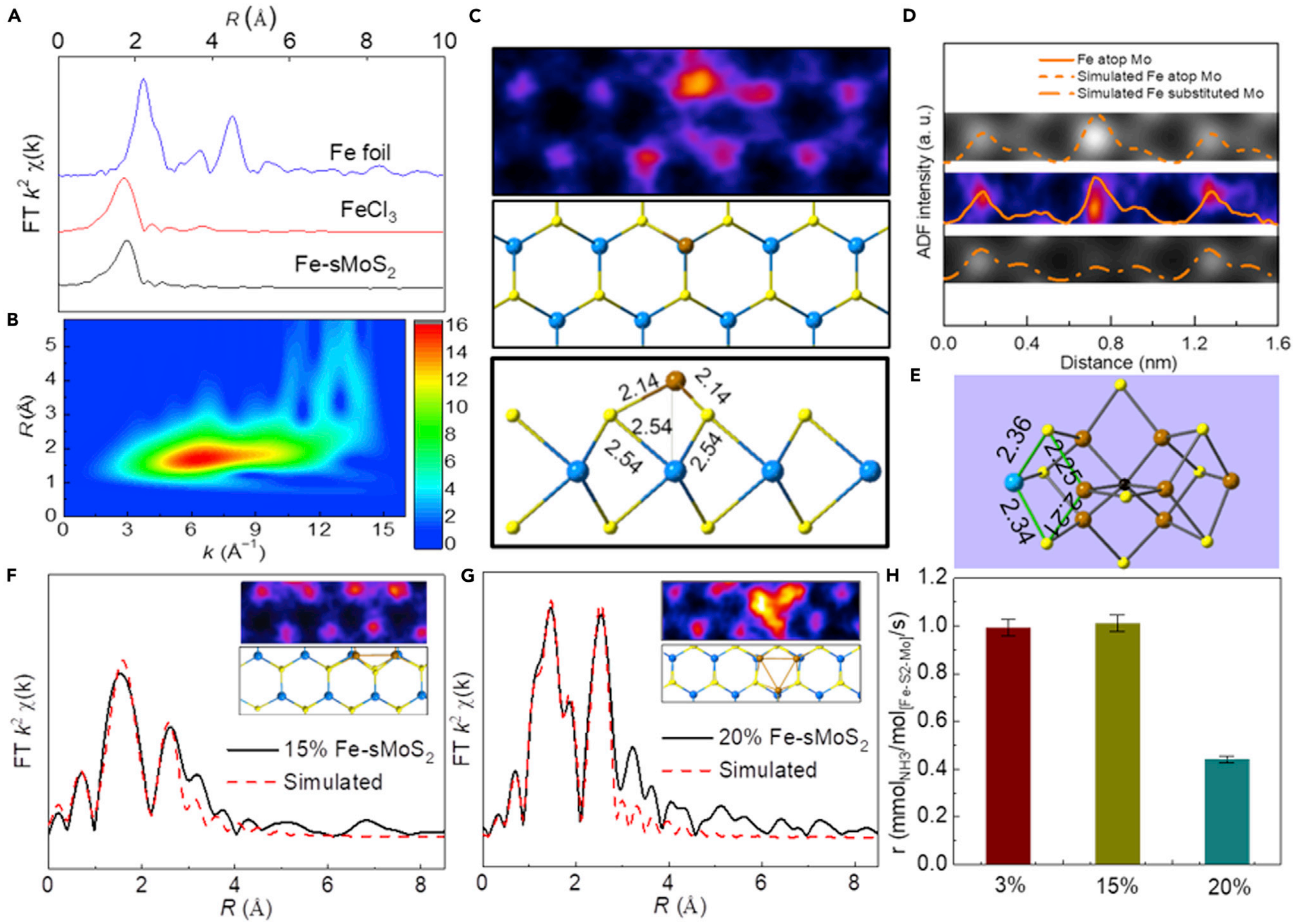

Figure 3. Structural analysis of Fe-sMoS_2 and core structure of FeMoco in nitrogenase

(A) Fourier-transformed magnitudes of Fe *k*-edge EXAFS spectra of Fe-sMoS_2 (3 wt %) samples.

(B) Wavelet transformation for the k^3-weighted Fe *k*-edge EXAFS signals of Fe-sMoS_2 based on Morlet wavelets at the first and higher coordination shells. The intensity reflects the content of the scattering signal.

(C) Atomic-resolution HAADF-STEM image of a single Fe on a Mo atop site of the basal plane of sMoS_2 (top) and atomic model from optimized DFT of a single Fe on a Mo atop site from a top view (middle) and a side view (bottom). The trigonal prismatic arrangement of bright-spot Mo atoms (2-H MoS_2) can be seen. The brightest dot is derived from an Fe_1 atom located atop a Mo atom. The four-membered ring motif of [Fe-S_2-Mo] in Fe-sMoS_2 is shaded with green lines.

(D) HAADF-STEM image (middle) and simulated images for Fe on a Mo atop site of MoS_2 (top) and Fe-substituted Mo site of MoS_2 (bottom). The lines along the images represent relevant ADF profiles.

(E) Atomic model FeMo-S cluster in FeMo cofactor of FeMoco. The same four-membered ring motif of [Fe-S_2-Mo] in FeMoco is shaded with green lines. Brown, black, blue, and yellow balls represent Fe, C, Mo, and S atoms, respectively. The value represents the bond length of FeMoco and Fe-sMoS_2 in angstroms. These values show the closed structure of the unit of [Fe-S_2-Mo] in Fe-sMoS_2 and that in FeMoco.

(F and G) Fourier-transformed magnitudes of Fe *k*-edge EXAFS spectra of Fe-sMoS_2 samples with a higher Fe loading of 15 wt % (F) and 20 wt % (G). The inset images show atomic-resolution HAADF-STEM of a surface Fe_2-S cluster on a Mo atop and vacant sites of the basal plane of sMoS_2 (top) and an atomic model from optimized DFT of a Fe_3-S cluster on Mo atop sites from top view (bottom). The dashed lines show the best simulated results using their inset models with units of [Fe_2-S_2-Mo] and [Fe_3-S_2-Mo].

(H) The yield of ammonia per mole of Fe synthesized over Fe-sMoS_2 with different Fe loadings at 270°C with 6 bar in water. Error bars indicate the standard deviations in activity measurements (similar to Figures S24 and S28).

compared them with the typical obtained STEM (middle) by their annular dark-field (ADF) profiles. The Fe atom appears as a bright dot on the atop Mo site. On the contrary, the ADF appears to be much darker for the Fe-substituted Mo site (Figure 3D). Clearly, the ADF profile for the model of Fe attached on the atop Mo site more closely resembles the image obtained from HAADF-STEM but shows significant deviations from the simulated model of Fe substituted Mo site, confirming the Fe atom on the atop Mo site as the frequently observed site. A similar structure was obtained for Co- and Ni-doped $sMoS_2$ at comparable doping levels (Figure S19). As shown in Figure S20, the X-ray absorption near-edge structure spectrum of quenched Fe-$sMoS_2$ from photocatalysis is drastically different from that of metallic Fe (Fe^0), but its absorption edge in the right-shift position between $Fe^{II}Cl_2$ and $Fe^{III}Cl_3$ implies that the average working oxidation state is between them for the anchored Fe. Of particular interest is a characteristic peak below the absorption edge of the Fe-$sMoS_2$. Fe foil containing surface FeO_x shows a similar asymmetric feature. It is well known that this pre-edge feature is due to a 1s → 3d allergically orbital forbidden transition that would be excluded by dipole selection rules for a symmetry site.[23] The observed pre-edge peak matches with the characterization isolated Fe_1 on $sMoS_2$.

The molecular models of Fe-$sMoS_2$ and FeMoco are shown in Figures 3C and 3E, respectively. Interestingly, the derived Fe–S, Mo–S and Fe–Mo bonding lengths of the [Fe-S_2-Mo] in this single-layer molecular catalyst are close to that of the reported molecular [Fe-S_2-Mo] unit in FeMoco from single-crystal data within the average deviations of 10% (Table S3 and Figures 3C, 3E, and S16).[23] Moreover, this Fe-$sMoS_2$ with [Fe-S_2-Mo] is active in converting N_2 to NH_3 and H_2 via photoactivation to provide excited electrons for the N_2 fixation in H_2O, mimicking the natural chosen nitrogenase as shown in Figures 1B and 1C.

Similarly, an additional EXAFS peak at a higher distance of ~2.5 Å is clearly found when the Fe loading is increased to 15 and 20 wt %, as shown in Figures 3F and 3G, respectively. This peak is ascribed to the Fe–Fe bonds in the formation of surface Fe-S interactions at these Fe loadings. From the HAADF-STEM images, similar to Fe_1, two Fe and three Fe atoms are found near the top of neighbor Mo sites. Fe clusters may also be located on one Mo site; however, in this case, the structure is not as stable as that on the top of neighbor Mo sites (Figure S21). Based on the simulated results of EXAFS with DFT calculations, Figures 3F, 3G, and S22 also show the corresponding surface Fe_2-S clusters and Fe_3-S clusters with bond lengths comparable to those of the free Fe-S structures with minimal surface reconstructions (Tables S4 and S5). The above results do not directly imply that discrete Fe-S clusters are specifically made on the MoS_2 surface at a particular Fe loading but perhaps are indicative of the most populated species, as seen by the corresponding HADDF-STEM images. Further deconvolution and quantification of EXAFS simulations and imaging to resolve their surface distributions are necessary. Nevertheless, the high affinity for Fe by the surface sites of MoS_2 for the high surface dispersion is clear, and the modeled Fe_1, Fe_2, Fe_3, and further Fe_4 S species contain the basic [Fe-S_2-Mo] motifs. Figure 3H shows the activity rank per mole of Fe in the 3, 15, and 20 wt % loadings. The latter highest-loading sample appears to suffer from aggregation, leading to a significantly lower activity of the surface motifs. As demonstrated in the mechanism of ammonia synthesis by enzyme, Fe-S protein in nitrogenase delivers the generated electrons to the catalytic MoFe protein by a remote outer-sphere mechanism.[8] Hereby, the surface Fe clusters may also play similar roles in electronic transfer and ammonia synthesis, mimicking the functional behaviors of enzymes in biofixation of nitrogen.

In addition, we studied the used catalyst at 3% loading after a long test in Figure S3 by EXAFS (Figure S23). As seen, the feature of single-atom Fe for the used catalyst with a single peak at the first shell is still sustained. No clear Fe–Fe bond can be identified in the post-sample with reference to the Fe foil. This result clearly indicates that the catalyst has a good degree of stability.

Mechanism underlying selective ammonia photosynthesis

To prove the unique feature of [Fe-S_2-Mo] in photocatalytic ammonia production, we compared the activities of MoS_2 and some selected first-row transition metal analogs at the lowest loading at room temperature, the results of which are shown in Figure S24. Bulk MoS_2 is shown to be inert for N_2 reduction, presumably because its CB is more positive than that of the N_2/NH_3 redox couple[21] (Figure S25). Reducing the layers of MoS_2 gradually enhances the activity for nitrogen fixation to ammonia. It has been proved that the band gap of MoS_2 could be enlarged by a more negative CB edge striding over the N_2/NH_3 redox couple.[24,25] In addition, indirect band excitation over few-layer MoS_2 can be switched to a more efficient direct band excitation for single-layer MoS_2.[26] While the single-layered MoS_2 materials display a negligible activity in H_2/O_2 splitting from water by visible light, a substantially higher photocatalytic ammonia production rate is recorded. Notably, the introduction of the [Fe-S_2-Mo] motifs into the basal planes of single-layered MoS_2 displays a far superior activity for ammonia and stoichiometric oxygen production from N_2 and H_2O reaction in the visible-light regime, thereby functionally mimicking FeMoco.

To appreciate the role of Fe, we evaluated and compared other first-row transition metals (Mn, Co, and Ni). Surface areas were measured on the basis of Brunauer-Emmett-Teller theory, and the result in Table S6 does not show any correlation between surface area and activity; hence, it is not the main factor affecting the photocatalytic performance. No clear feature of transition metals can be found from the XRD patterns of metal-sMoS_2 (Figure S26A), and the electron paramagnetic resonance (EPR) signal is greatly attenuated after the introduction of transition metals (Figure S26B), indicating that some metal atoms take up the S vacant sites of the sMoS_2 (most metal atoms are at the atop Mo sites as found by STEM). Time-resolved photoluminescence (TRPL) spectra of sMoS_2 and Mn-, Fe-, Co-, and Ni-doped sMoS_2 are also shown in Figure S27. As seen from the TRPL spectra, the instantly generated excited electrons and holes in sMoS_2 are annihilated rapidly within a few nanoseconds. Doping single transition-metal atoms onto this structure at the lowest loading apparently prolongs their recombination time, suggesting that the metal exerts an enhanced degree of charge separation by accepting excited electrons. Mn- and Ni-doped sMoS_2, followed by Co-sMoS_2, show a similar exciton lifetime. Interestingly, Fe-doped sMoS_2 with optimal d-band filling and position also gives the longest exciton lifetimes with the slowest photoluminescence (PL) decay curves. Notably, the rank of their lifetimes (Table S7) shows a strong inverse relationship with photocatalytic activity for ammonia production (Figure S28). It is anticipated that the prolonged exciton lifetime is critical in allowing chemical reactions of the excitons to occur before they recombine by relaxation, leading to photocatalytic N_2 fixation. Thus, the Fe-doped sMoS_2 with the Fe-S_2-Mo motifs displays the best combination of metal site and "electron relay" components for charge separation analogous to that in the biological system.

For N_2 activation over nitrogenase, it was suggested from theoretical calculations that N_2 could linearly bind to either the Mo atom over the distal pathway (hydrogenation starts at terminal N) or the Fe atom over the alternating pathway (hydrogenation starts at N in proximity to Fe) in FeMoco.[10] We then modeled the electron states of highest occupied molecular orbital (HOMO) and lowest unoccupied molecular orbital (LUMO) and band structures in Mn-, Fe-, Co-, and Ni-doped sMoS_2 (Figures 4A and S29). The HOMO and LUMO orbitals concentrate on the edge of sMoS_2 with relatively low electron delocalization, verifying the highly active edge site of sMoS_2 as reported in the literature.[27] Transition-metal atom doping distinctly improves the

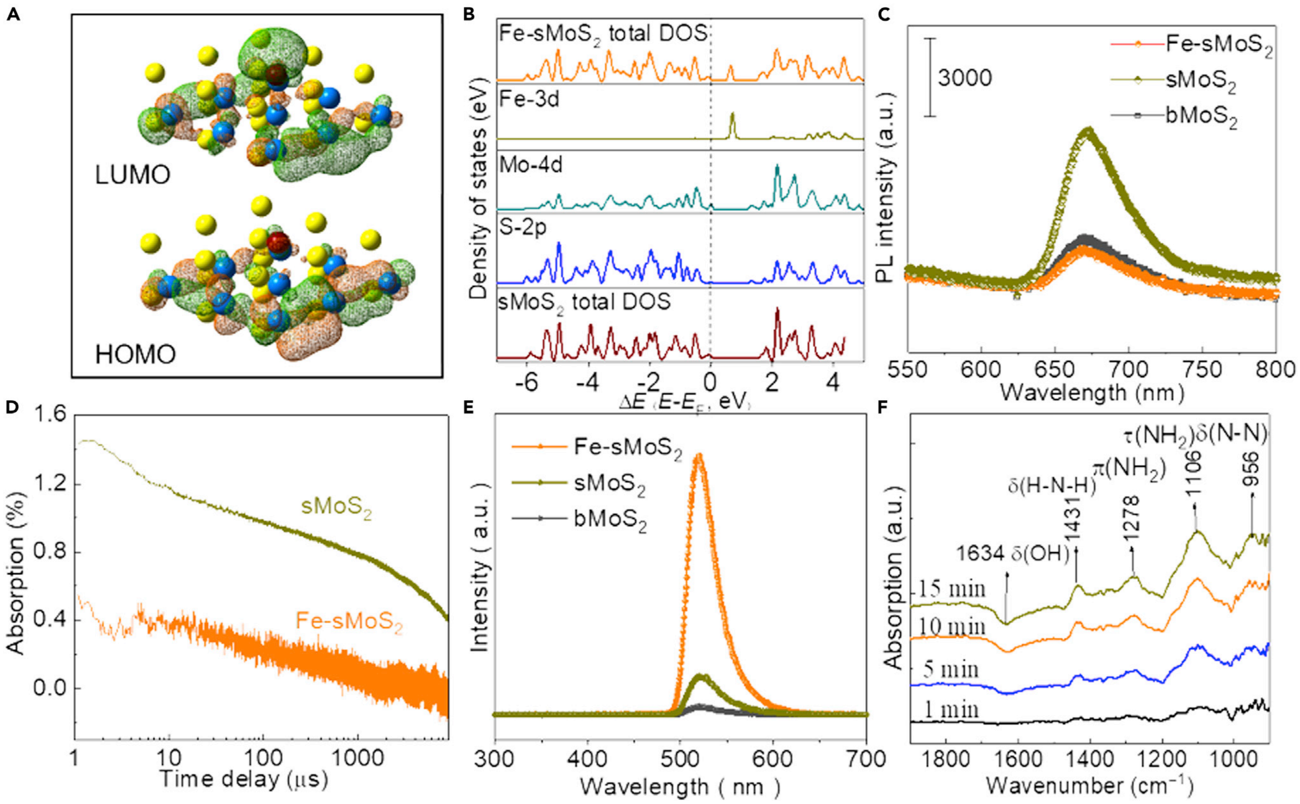

Figure 4. Proposed electron-hole transfer route for associative nitrogen fixation over an Fe-S_2-Mo unit

(A) Calculated HOMO-LUMO states of Fe-sMoS_2. The green net represents a positive electron density, and brown represents a negative electron density.

(B) Total and partial density of states for sMoS_2 and Fe-sMoS_2.

(C) PL spectra over bMoS_2, sMoS_2, and Fe-sMoS_2 (3 wt %).

(D) TAS delay profiles for sMoS_2 and Fe-sMoS_2 (3 wt %).

(E) Fluorescence profiles for bMoS_2, sMoS_2, and Fe-sMoS_2 (3 wt %).

(F) Time-resolved ATR-FTIR spectra at a flow of N_2 and H_2O over Fe-sMoS_2. Time zero was set when light illumination started.

degree of delocalization of the frontier orbitals, especially to their LUMO orbitals, and the frontier orbital delocalization follows the order Fe > Co > Mn ≈ Ni. The higher degree of delocalization indicates the more stable population of photoexcited electrons in LUMO orbitals, thus accounting for the longer lifetime for the recombination of excited photogenerated electrons and photogenerated holes. This is in good agreement with the TRPL experimental results. Among them, the LUMO orbital distribution over the Fe atom in Fe-doped sMoS_2 should be noted (Figure 4A). In particular, they demonstrate that excited electrons could be transferred from the VB to the CB of sMoS_2 via the conductive Fe-S_2-Mo motifs and reside on the Fe atom during the photoexcitation process to enter into the anti-bonding orbital of an absorbed N_2 molecule and thus facilitate the hydrogenation reaction of N_2 for ammonia production. The partial density of states (DOS) was analyzed to explore the contributions of Fe 3d, Mo 4d, and S 2p orbitals to the CB and VB. As shown in Figure 4B, the band gap of sMoS_2 is about 1.7 eV. Doping of Fe results in new energy states as the CB at 0.73 eV above the Fermi level; partial DOS analysis verified that Fe 3d orbital contributed mainly to this lowest CB, demonstrating that the photogenerated electron will concentrate on the Fe species for the activation of N_2 molecules. On the other hand, the DOS calculation indicates a smaller band gap (Figures 4B, S30, and S31) for Fe-doped sMoS_2 relative to other catalyst materials, which is also favorable for electron transfer from HOMO to LUMO orbitals by photoexcitation.

To study the dynamics of photocatalysis (generation and quenching of photoinduced electron and hole), we then explored the optical structure of Fe-sMoS_2. UV-visible (UV-vis) spectroscopy was performed to reflect the band gap by Tauc plots (Figure S32 and Note S1). The obtained band-edge positions are shown in Figure S33, indicating that photoexcitation can overcome both barriers for ammonia synthesis and water splitting over Fe-sMoS_2. To prove the generation of photogenerated electrons and holes, we also conducted PL spectroscopy, transient absorption spectroscopy (TAS), and fluorescence spectroscopy, the results of which are shown in Figures 4C–4E. The PL signals of semiconductor materials result from the recombination of photoinduced charge carriers. In general, the lower the PL intensity, the lower the recombination rate of photoinduced electron-hole pairs and the higher the photocatalytic activity of semiconductor photocatalysts.[28] This coincides with our experimental results. Fe-doped sMoS_2 shows a lower PL signal but higher activity than sMoS_2. Similarly for the TAS, Fe-sMoS_2 shows a poorer transit absorption signal from the first excited state (laser pumped) to further higher states than that of non-promoted sMoS_2 as a result of the capture of electrons by Fe (Figure 4D). To confirm the generation of holes, we measured the formation of the one-electron-oxidation product, OH, by a coumarin fluorescence probe method. Upon photoirradiation of the sMoS_2 and Fe-sMoS_2 suspensions in the presence of coumarin, a stronger fluorescence band attributable to the OH adduct of coumarin, umbelliferone, was observed for Fe-sMoS_2, insinuating a higher efficiency to generate holes.

We also studied the dynamic N_2 reduction to NH_3 over Fe-sMoS_2 (3 wt %) by using *in situ* attenuated total reflection Fourier transform infrared (ATR-FTIR) with light illumination (Figure S34). The infrared (IR) absorption bands of 3,303 and 1,634 cm^{-1} shown in Figures S35 and 4F can be attributed to the O–H stretching and H–O–H bending of adsorbed water molecules, respectively, on the catalyst structure. Their decreasing signals from background are a result of the consumption of the adsorbed water molecules upon light illumination in N_2. Simultaneously, four bands at 1,431, 1,278, 1,106, and 956 cm^{-1} arise, and these can be attributed to the H–N–H bending, –NH_2 wagging, –NH_2 twisting, and N–N stretching of adsorbed N_2H_y ($2 \leq y \leq 4$) species, respectively.[29] We further analyzed the content of hydrazine (the by-product of associative N_2 fixation with NH_3) by using *para*-(dimethylamino) benzaldehyde acidic solution, which gave a small but detectable peak at around 450 nm upon UV-vis spectroscopy, as shown in Figure S36. This indicates the formation of N_2H_4 (<1%) from N_2 reduction, which forms a complex with the benzaldehyde compound.[30] Thus, Fe-sMoS_2 appears to undertake the same association pathway for N_2 fixation as that of nitrogenase, where both structures contain the common motifs of four-membered [Fe-S_2-Mo] rings.

The electronic interaction between Fe with MoS_2 may be reflected from the change in bond distance between Fe and S atoms. We optimized the structure of Fe-MoS_2 as well as N_2-adsorbed Fe-MoS_2. As shown in Figure S37B, when N_2 binds on the Fe site the Fe–S bond length simultaneously extends from 2.14 to 2.20 Å. The FeS clusters are known to be able to mediate from electron-rich to electron-poor regions. The light illumination will promote excited electrons from the monolayer MoS_2 structure to N_2 via its adsorption on immobilized Fe while the degree of electron back-donation from Fe to attached S (ligands) will then be decreased, hence producing longer Fe–S bond length. This result clearly demonstrates that the activation of N_2 is significantly affected by the electronic interactions between Fe and MoS_2.

It is generally recognized that ammonia synthesis at nitrogenase follows an associative pathway without breaking N≡N triple bonds directly in the transition state.[8–10] N_2 adsorption and the subsequent first proton and electron reactions of adsorbed N_2 (formation of $*N_2H$) are two key steps in this non-dissociative reduction of N_2.[8] According to our DFT calculations shown in Figure S37, N_2 is adsorbed on the Fe atom in [Fe-S_2-Mo] as the end-on mode spontaneously. The energy plots in Figure S38 show that the first hydrogenation step, in which a hydrogen atom is added, is the most challenging step because the energy is going uphill. Hydrogenating the proximal N to Fe is less favorable with a higher energy state, whereas the species from hydrogenating the terminal N is relatively stable. The following hydrogenation steps can be separated into two pathways, distal and alternating, as shown in Figure S38. The intermediate species via the latter pathway is more stable than that via the former pathway. According to the energy plots, the nitrogen fixation to ammonia over [Fe-S_2-Mo] sites through the alternating pathway appears to be more energetically favored despite the higher activation barrier in the first hydrogenation step. Caution is necessary because recent organometallic mimics suggest that there could be a dynamic equilibrium between the partial hydrogenated intermediates for the two N in the bound N_2.[8] In addition, the energetics for adding a hydrogen atom to bound N_2 could be different from adding a proton and an e^- such that the latter is limited by the light illumination process. The nitrogen fixation to ammonia on Fe_1 over [Fe-S_2-Mo] finally appeared to go through the alternating pathway (Figures 4F and S38), indicating the similarity in mechanism for both non-biological and biological processes in ammonia synthesis.

The roles of heat and light

From the experiments, we note that the reaction temperature can significantly affect the activity and selectivity (Figures 1B and 1C). Figure 5A shows that the electron enriched on the Fe site prefers transferring to the adsorbed N_2 rather than to H as long as the temperature is below 180°C (exclusive selectivity to NH_3): the higher the temperature used, the higher the activity that is obtained. However, H^+ from water (H_3O^+) begins to accept electrons at 180°C to form H_2, and this process becomes faster when the reaction temperature is higher than 180°C. These results insinuate the competition between N_2 and H reduction for the excited electrons. To assess the contributions of heat and light, we evaluated the catalytic performance by using different light wavelengths (Figure 5B) at room temperature and 270°C. The wavelength of the light source significantly affects the activity of ammonia production, and the activity for light with longer wavelength, especially above 700 nm (near-IR), drops significantly. These results suggest that the light providing the photoexcited electrons can directly promote the activity and that the heat alone cannot influence the activity of Fe-sMoS_2 much. As a result, the use of elevated temperature appears to affect the subsequent reaction steps after the initial photoelectron excitation to N_2* is facilitated by the thermal mean. Interestingly, Figures 5C and S39 and Table S8 also show that the elevated temperature significantly prolongs the exciton lifetime and suppresses electron-hole pair recombination in Fe-sMoS_2 (3 wt %). Similar longer exciton lifetimes at higher temperatures can be found for some other materials (e.g., InAs/GaAs and InGaN/GaN) as a result of exciton delocalization by thermal energy.[31–33]

Because ammonia synthesis and water splitting are clearly interwoven under our conditions at elevated temperatures, the selectivity to ammonia or hydrogen must be the result of the competition for excited electrons from the adsorbed N_2 and H_2O (H^+). From the DFT calculations (Figure 5D), the result shows that wherever N_2 (H_2O) is placed on an Fe_1 atom-doped sMoS_2 slab, the N_2 (H_2O) adsorption

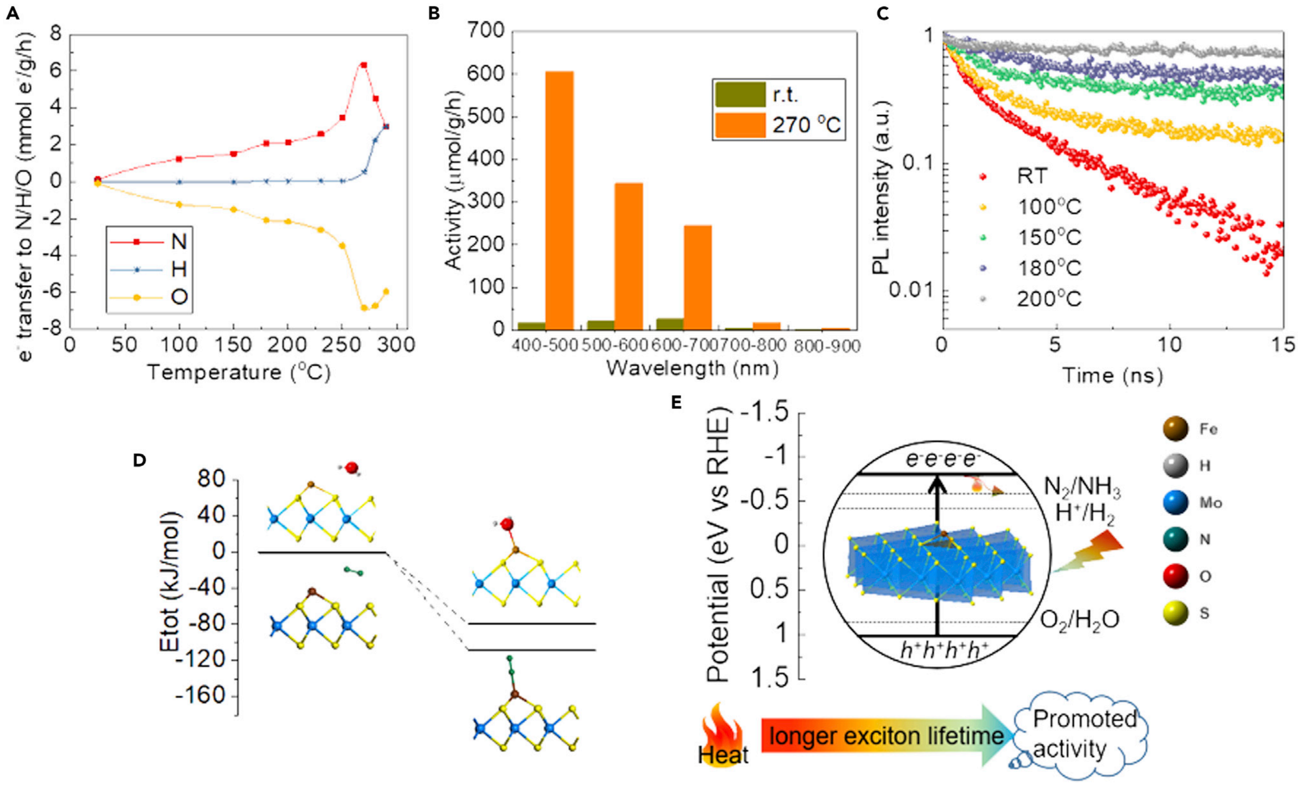

Figure 5. Roles of heat and light over Fe-sMoS_2 (3 wt %)

(A) Amount of exciton (e^-) transfer into N, H, and O as a function of temperature. A minus value means the transfer is to holes.

(B) Catalytic performances under different light wavelengths.

(C) Time-resolved normalized photoluminescence intensity as a function of temperature, as measured with a pulsed Ti:sapphire laser (~150 fs).

(D) Energy plot of N_2 and water adsorption on Fe-sMoS_2 from DFT calculations with reference to the energies of Fe-sMoS_2 and free N_2 and a water molecule.

(E) Correlation of activity with heat and light at pH 7. We can see that light directly affects the activity of ammonia synthesis through photoexcitation and that heat indirectly affects the activity through subsequent rate enhancements and prolonged exciton lifetime.

always converges onto the Fe_1 atom in [Fe-S_2-Mo] as the end-on mode spontaneously. However, the adsorption energy of N_2 on Fe-sMoS_2 is higher in magnitude than that of H_2O on Fe-sMoS_2, indicating that the kinetic N_2 adsorption is more favorable. This could be the reason why the selectivity for N_2 reduction is always higher than that for H_2 production at temperatures up to 180°C. As temperature further increases, it causes significant attenuation in the population of N_2 chemisorption over Fe-sMoS_2 (Figure S40), and thus more active sites of Fe could be available for the more excessive proton reduction from water. In addition, from the thermodynamic values in Figure 1, we can see that water splitting becomes relatively more thermodynamically favored than ammonia synthesis when approaching closer to the equilibrium values. Thus, the use of higher temperature beyond 270°C will render water splitting more favorable than ammonia synthesis, leading to the increase in selectivity of H_2.

From our exciton lifetime experiments, we find that the H^+ from water cannot combine with excited electrons until the lifetime of the excitons in the catalyst is longer than 12 ns, whereas the N_2 can even be achieved in 3 ns (Figure S41). We attribute this to the ready N_2 adsorption on the Fe atom that can capture excited electrons in relatively shorter time. In addition, if the stronger electronegative N_2 moiety is taken up by the Fe_1 atom, excited electrons during visible-light illumination are

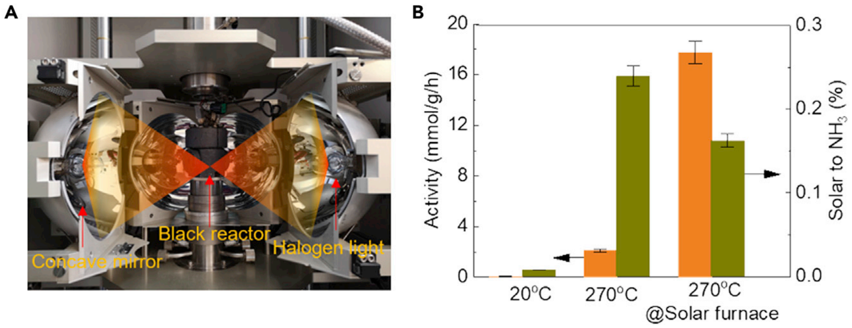

Figure 6. Photocatalytic ammonia synthesis in a solar furnace

(A) Photograph of a four-mirror floating-zone solar furnace from Crystal Systems used to mimic a solar concentrator to focus a light beam to provide both heat and photons to the Fe-sMoS$_2$ (3 wt %) without any other energy input from an electrical device.

(B) Activity of ammonia synthesis and solar-to-ammonia energy efficiency under different conditions. For the test in the solar furnace, a reactor temperature of 270°C is maintained with 6 bar of N$_2$ in water. Error bars indicate the standard deviation.

expected to be retained to further prolong the exciton lifetime for subsequent proton reduction to ammonia on the N$_2$-Fe$_1$ against the typical fast recombination of excitons from this layer structure, which substantially promotes the N$_2$-to-NH$_3$ reaction over H$_2$O photolysis without being in contact with nitrogen gas (Figure S42). As a consequence, the adsorption of N$_2$ and the reaction temperature can promote the photosynthesis of ammonia. Thus, all the results clearly indicate the strong interplay between the photo and thermal contributions to the overall enhancement in the ammonia production rate (Figure 5E).

Evaluation of feasibility and scalability

Large-scale application of particulate photocatalytic systems has attracted increasing attention recently because it costs less than photovoltaic-powered electrolysis and photoelectrochemical processes, as well as the fact that complicated reactor structures are not required.[34–36] Therefore, to demonstrate the technical feasibility of using solely renewable light energy to supply the required thermal heat and visible photons for photocatalytic ammonia synthesis in this new process, we used a solar furnace to mimic the solar light concentrator without any direct thermal energy input from an electrical device (Figure 6A). The reactor temperature of 270°C was maintained by this solar source with black-body radiation, and an ammonia production rate of about 17 mmol g^{-1} h^{-1} with an energy efficiency of 0.18% was achieved over Fe-sMoS$_2$ (3 wt %) with the *in situ* solar furnace (Figure 6B). Although the energy efficiency is a little lower than that of 0.24% seen with a lab-based light source and electric heating, it is an order-of-magnitude improvement over room-temperature ammonia synthesis. The productivity is sufficient to cover more than 66 m^2 of farmland per gram of catalyst if a leaching rate of 100 kg N ha^{-1} for a selected crop is used (see Note S1).[37] In addition, 3% Fe-MoS$_2$ was also evaluated in a fixed-bed reactor (Figure S43). As shown, the yields are much higher at 270°C than those at room temperature. Without the light illumination, the yield would not be sustained. Apparently, high reaction temperature and light are the two key parameters for the efficient ammonia synthesis. The flow-reactor study indicated that the catalyst is still workable for ammonia synthesis under a flowing mode.

Conclusions

In conclusion, a bio-inspired solid structure consisting of [Fe-S$_2$-Mo] four-membered rings on a 2D single layer of MoS$_2$ has been synthesized. The material functionally mimics the nitrogenase enzyme, which shows a strong ability to reduce N_2 to NH_3 in aqueous solution under mild conditions with visible-light illumination, whereby excited electrons from the $sMoS_2$ slab are conducted to the redox active Fe-S sites through the [Fe-S_2-Mo] as the electron relay units. Elevation of reaction temperature and adsorption of N_2 can prolong the exciton lifetime and further boost the NH_3 harvest. From DFT calculations and ATR-FTIR analysis, the [Fe-S_2-Mo] motif is clearly shown to carry out an associative mechanism in converting N_2 to NH_3. N_2 prefers to bind linearly on the Fe atom in the [Fe-S_2-Mo], which will undergo stepwise hydrogenations to NH_3 with the successive formation of hydrogen atom from H^+/e^- pairs. Thus, the photocatalytic method for ammonia synthesis over this type of material, although small in quantity, could open up an exciting possibility for the decentralization of ammonia supply for the provision of fertilizer to local farmlands.

EXPERIMENTAL PROCEDURES

Resource availability

Lead contact

Correspondence and requests for materials should be addressed to the lead contact, Shik Chi Edman Tsang (edman.tsang@chem.ox.ac.uk).

Materials availability

This study did not generate any new unique reagents or materials.

Data and code availability

This study did not generate codes, software, or algorithms.

Materials

Materials included Fe(II) acetate (>99.99%, Alfa Aesar), MoS_2 (Sigma-Aldrich), $FeCl_3 \cdot 6H_2O$ (reagent grade, Alfa Aesar), $FeCl_2$ (98%, Sigma-Aldrich), *n*-butyllithium/hexane (1.6 M, Sigma-Aldrich), polyvinylpyrrolidone (PVP, reagent grade, Sigma-Aldrich), isopropanol (99.9%, Sigma-Aldrich), HCl (≥98%, Sigma-Aldrich), copper(II) acetate (98%, Sigma-Aldrich), manganese(II) nitrate hydrate (98%, Sigma-Aldrich), cobalt(II) acetate tetrahydrate (reagent grade, Sigma-Aldrich), nickel(II) acetate tetrahydrate (98%, Sigma-Aldrich), and FeS (99.9%, Sigma-Aldrich).

Synthesis of few-layered and single-layered MoS_2

Few-layered MoS_2

Bulk MoS_2 powder was first dispersed in 400 mL of water/isopropanol (1:3, v/v), and then 4 mL of hydrazine monohydrate was added into the solution. The obtained mixture was subsequently placed into a sonication bath for 12 h for chemical exfoliation, followed by centrifugation at 2,000 rpm for 1 h. The supernatant collected was then filtered with vacuum filtration, followed by washing with deionized (DI) water. Finally, the exfoliated product was dried under vacuum for 24 h.

Single-layered MoS_2

Bulk MoS_2 powder was soaked in 1.6 M *n*-butyllithium/hexane under nitrogen atmosphere for 48 h. Subsequently, solid Li_xMoS_2 was isolated by vacuum filtration and washed with hexane to remove excess *n*-butyllithium. The obtained product was immersed in DI water and sonicated for 12 h and then centrifuged twice at 5,000 rpm for 15 min. The supernatant collected was then filtered via vacuum filtration and then washed with DI water. The exfoliated product was finally dried under vacuum for 24 h.

Synthesis of metal-atom-doped $sMoS_2$

A metal precursor solution was prepared by dissolving 0.2 mM Fe(II) acetate into 1 mL of 0.5 mM thiourea solution and aged overnight to form a homogeneous metal complex. A specific amount of metal complex solution based on the loading was then mixed with 30 mL of colloid solution, which was made by dispersing $sMoS_2$ in water/isopropanol (1:3, v/v) and PVP (stabilizer, 50 mg). The mixture was then transferred to an autoclave and subsequently placed in an oven at 160°C for 24 h. Thereafter, the precipitate was washed several times with DI water and dried under vacuum for 12 h to yield the final solid product. The single doped-metal content was controlled at around 3 wt % with error ±0.5 (Fe 3.3 wt %, Co 3.0 wt %, Ni 3.5 wt %). Their metallic source can be found in the "materials" section. Fe loading was then further increased to 15 and 20 wt % to give 10% Fe-$sMoS_2$ and 15% Fe-$sMoS_2$, respectively.

HAADF-STEM

The finely ground samples were firstly dispersed in ethanol and then sonicated for 0.5 h. Thereafter, the solution was dropped and dried onto the holey carbon-coated Cu-TEM grid for analysis. The analysis was performed by a JEOL-JEM2100 aberration-corrected transmission electron microscope located in Birmingham, UK. A low voltage of 60 kV was applied for the imaging to avoid beam excitation and damage. Off-axis annular detector imaging was used for dark-field (*Z*-contrast) imaging and atomic-resolution imaging. Compositional analysis by X-ray emission detection was also conducted. For energy-dispersive X-ray spectroscopy, a Bruker 5030 SDD detector with a window area of 30 mm^2 was used. All results were then processed with Esprit 2.0 software.

Inductively coupled plasma spectroscopy

The finely ground samples were dissolved and diluted with 5 wt % HCl for inductively coupled plasma analysis, which was performed by an optical emission spectroscope (Optima2100DV, PerkinElmer).

EXAFS

Fe *k*-edge and Mo *k*-edge X-ray absorption spectroscopy (XAS) was conducted in fluorescence mode at the BL07A XAS beamline at the National Synchrotron Radiation Research Center in Taiwan. For examination of the local chemical environment around Fe and Mo atoms, EXAFS data were extracted from XAS spectra. The Demeter ATHENA program was used for EXAFS data analysis, whereby the data were background subtracted, normalized, and Fourier transformed. The Demeter ARTEMIS program was used to perform the least-squares curve-fitting analysis of the EXAFS $\chi(k)$ data (Figure S44). EXAFS wavelet analysis was performed according to the protocol and calculations developed by Funke and colleagues, whereby the backscatter atoms are distinguished within the same atomic shell.[38] To confirm the reproducibility of the experimental data, at least two scan sets were collected and compared for each sample. The spectra were calibrated with Fe and Mo foil as a reference. The amplitude reduction factor was obtained from analysis of the Fe and Mo foil, which was used as a fixed input parameter to allow refinement in the coordination number and bond distance of the absorption element.

EPR

Continuous-wave EPR spectra were operated by an X-band (9.4 GHz) Bruker EMX EPR spectrometer. Then X-band spectra were measured over a 300 gauss field range, and the data were collected with 15 scans.

XPDF

XPDF was operated at Beamline I15-1 at the Diamond Light Source in Harwell, UK. Scattering data were collected at relatively high scattering angles with high-energy powder diffraction. The PDF data were generated by Fourier transform.

Surface-area measurements

Specific surface areas were collected by a Micromeritics Tristar II analyzer by measuring the N_2 adsorption and desorption at 77 K. Samples were first degassed at 110°C for 12 h prior to each measurement.

N_2 chemisorption

The amount of N_2 chemisorption is based on the difference between sequential adsorptions conducted on a Micromeritics ASAP 2020Plus analyzer. An initial isotherm was measured in a pressure range of 300–600 mmHg to obtain the total sorption (chemical and physical sorption). A 30min evacuation was conducted to remove the reversibly physical adsorbate molecules on the catalyst surface prior to measuring a repetitive isotherm under the same conditions as the initial one. The average difference between the initial and repetitive isotherms reflects the uptake of the irreversibly chemisorbed adsorbates on catalysts.

TAS

Microsecond transient absorption decays were acquired in absorption mode with a home-built setup. A Nd:YAG nanosecond laser (LAB-130-10, Spectra-Physics) was used as the pump light, and the 355 nm output light was focused on the MoS_2 samples. Typical excitation densities of 1 mJ cm^{-2} and the laser repetition rates of 10 Hz were used. Probe light was generated by a 100 W ASBN-W tungsten-halogen lamp. Long-pass and short-pass filters were positioned between the lamp and sample to minimize the short-wavelength irradiation and heating of the sample. Absorption changes from the sample were collected and relayed to a monochromator (Spectral Products CM110) to select the probe wavelength. Time-resolved intensity data were collected with a Si photodiode. The signal was amplified by a wide-band preamplifier and recorded by an oscilloscope (Tektronics DPO4012). Transient absorption decays were typically obtained from the average of 128 laser pulses, and samples were probed at 900 nm. Typically, 2 mg mL^{-1} MoS_2 powders were dispersed in aqueous solution and transferred to 2-mm-path-length cuvettes for measurement. Samples were stirred prior to the start of each kinetic acquisition.

Fluorescence spectroscopy

Fluorescence spectra were obtained to measure the amount of $^\bullet OH$. Sample powder (0.05 g) was first dispersed in 40 mL of 0.001 M coumarin aqueous solution. After stirring and irradiation for 1 h, the solution was centrifuged and the liquid was transferred into a Pyrex glass cell for the fluorescence measurement of 7-hydroxycoumarin through a spectrofluorometer (PerkinElmer LS 55) at 390 nm excitation wavelength and 460 nm emission wavelength.

Superconducting quantum interference device

Measurements of superconducting quantum interference were conducted by an MPMS-XL device (Quantum Design), which is cooled by liquid He. Samples were put in a capsule and transferred to the facility. The magnetic moment was collected at 5 K.

TRPL spectroscopy

Photoluminescence spectra and corresponding lifetime measurements of excitons were obtained from a bespoke micro-photoluminescence setup, in which a

Ti-sapphire laser (λ = 266 nm, pulse duration = 150 fs, repetition rate = 76 MHz) was directed onto the sample. Time-resolved measurements were performed with the spectrometer as a monochromator before the selected signal was passed to a photomultiplier tube detector with an instrument response function width of ~150 ps connected to a time-correlated single-photon counting module.

Parameters describing the photoluminescence were obtained by fitting the background-corrected PL spectra with a monoexponential decay function of the form $y = A_1\exp(-x/\tau_1) + y_0$ for $sMoS_2$. A double-exponential model using the equation $I(t) = A_1\exp(-t/\tau_1) + A_2\exp(-t/\tau_2)$ was applied when transition metal (Mn, Fe, Co, and Ni) was introduced.[39,40]

ATR-FTIR spectroscopy

In situ ATR-FTIR spectra were collected with a multiple-reflection ATR accessory (custom-modified GladiATR from PIKE Technologies) in a Varian 680-IR spectrometer controlled by Resolutions Pro software. A trapezoidal Si internal reflection element (Crystal GmbH, 8.39 × 5 × 1 mm^3) with a face angle of 39° was sealed into a polyether-ether-ketone baseplate with silicone sealant, and a custom cell was sealed on top.[41] A layer of water molecules, which were necessary to provide protons, was first preadsorbed on the surface from a drop of water onto the catalyst. Subsequently, 50 mL min^{-1} of N_2 saturated with H_2O was passed over the catalyst while the visible-light source was turned on, and the IR absorption was monitored with a mercury-cadmium-telluride detector over the course of the reaction.

UV-vis absorption spectroscopy

UV-vis absorption spectra were collected with a Varian 100 Bio UV-vis spectrometer in absorbance mode with a step interval of 1 nm. The solution after reaction overnight was filtered. The obtained 5 mL was mixed with 5 mL of 0.14 M *para*-(dimethylamino)benzaldehyde and 1 M H_2SO_4 solution and transferred into an optical glass cuvette for hydrazine measurement.

DFT theoretical calculations

All calculations were performed with first-principles DFT as implemented in the Vienna *ab initio* simulation package,[42] the exchange-correlation energy functional was described by the generalized gradient approximation with the Perdew-Burke-Ernzerhof (PBE) functional,[43] and the ion-electron interaction was treated with the projector-augmented wave (PAW) method[44] with a plane-wave cutoff energy of 400 eV. A (3 × 3) supercell of 2H-MoS_2 was selected to simulate $sMoS_2$, periodic boundary conditions were employed, and 15 Å of vacuum in the z direction was set to separate neighboring $sMoS_2$. The Brillouin zone was sampled with a 2 × 2 × 1 and an 8 × 8 × 4 Monkhorst-Pack[45] grid of *k*-points for geometry optimizations and orbital analysis calculations, respectively. Both lattice constants and atomic positions were relaxed until the forces on the atoms were less than 0.02 eV $Å^{-1}$ and the total energy change was less than 1.0×10^5 eV. To rationalize the different performance of $sMoS_2$ and transition-metal-doped MoS_2 in catalytic ammonia photosynthesis, we performed DOS and frontier orbitals topology analyses at the PBE/PAW level of theory.

Ammonia synthesis measurement

Without specific instruction, the photocatalytic activity experiments were conducted at ambient temperature with a 70 W tungsten lamp (Glamox Professional 2000) and UV light cutoff to simulate visible light. For the fixation of molecular nitrogen, 10 mL of Milli-Q water was added into the flask with 1 mg of photocatalyst after reduction, and the solution was transferred to an autoclave. Subsequently, the air in the autoclave was removed by purging with high-purity N_2 (purified by a Varian filter [Agilent CP17973] containing two gas-clean fillers for stepwise moisture and oxygen removal).[46,47] Therefore, the system was sealed with 6 bar of N_2 rather than a continuous process. The temperature was controlled by two heating bars assembled in the autoclave prior to the light illumination. During the light illumination, the catalyst was dispersed by stirring. The irradiation power in the center of the autoclave was measured to be 45 mW cm^{-2}. After light illumination for 1 h, the solution was taken out and filtered to remove the photocatalyst, and the concentration was monitored by colorimetry with the UV-vis spectrometer. For the measurement of ammonia yields, a specialized highly sensitive ammonia detector was used (Thermo Scientific Orion Ammonia Gas Sensing ISE Electrode). After the reaction, the catalyst was attached to the magnetic bar because of its magnetic property and was then collected for the stability tests. The amounts of hydrogen and oxygen were measured by a gas chromatograph equipped with thermal conductivity detectors with He and N_2 as respective carrier gases.

The final concentration of ammonia was determined by the selective ammonia electrode, through which ammonia gas can be permeated to the electrode and detected. The electrode uses a hydrophobic gas-permeable membrane to separate the sample solution from the electrode filling solution. Liquid does not penetrate the membrane holes. Dissolved ammonia in the sample solution diffuses through the membrane until the partial pressure of ammonia is the same on both sides of the membrane. In any given sample, the partial pressure of ammonia will be proportional to its concentration. The potential of the electrode sensing element with respect to the internal reference element is described by the Nernst equation $E = E_0 - S\log[NH_3]$, where E is measured electrode potential, E_0 is the reference potential, NH_3 is the ammonia concentration in solution, and S is the electrode slope. Prior to each test, the pH of all standards and samples is adjusted to above 11. The ammonia electrode responds to the partial pressure of dissolved ammonia gas. The partial pressure of dissolved ammonia gas is related to the ammonia concentration by Henry's law, $K_h = [NH_3]\text{aqueous}/P_{NH3} = 56$ moles per L-atm (25°C).

The apparent quantum efficiency measurements were carried out under a 300 W xenon lamp (Newport) through quartz windows of the same autoclave using bandpass filters of 432 ± 10 and 575 ± 25 nm. Numbers of photons were calculated from the irradiation powers in each wavelength region measured by a light meter at the corresponding wavelengths. The apparent QE can be calculated with the following equation:

$$\text{QE (\%)} = \frac{\text{number of ammonia molecules} \times 3}{\text{number of incident photons}} \times 100\% \text{ or } \frac{\text{number of hydrogen molecules} \times 2}{\text{number of incident photons}} \times 100\%.$$

The energy efficiency was calculated as solar to NH_3 with the following equation:

$$\text{solar to NH}_3\text{ (\%)} = \frac{[\Delta G \text{ for ammonia generation } (\text{J mol}^{-1})] \times [\text{ammonia formed } (\text{mol})]}{[\text{total input energy (W)}] \times [\text{reaction time (s)}]}.$$

The free energy for NH_3 generation from water and N_2, which varies with the reaction temperature, can be found in Figure 1. For example, ΔG at 270°C is 326 kJ mol^{-1}. The overall irradiance of the UV cutoff lamp is 45 mW cm^{-2}, and the irradiation area is 1.64 cm^2. Therefore, the power input over the irradiation area is therefore determined to be 74 mW. The solar to NH_3 for ammonia synthesis over Fe-sMoS_2 at 270°C for 1 h is

$$\frac{[326/1,000]\times\left[2,039.1\times10^{-6}\times10^{-3}\right]}{\left[45\times10^{-3}\times1.64\right]\times[3,600]}\times100=0.24\%.$$

Isotopic N_2 ($\geq$98%) was used to prove that the obtained ammonia derives from N_2 gas rather than some other sources. Indophenol assays were freshly prepared by adding 0.5 mL of aliquot solution after 1 h of reaction to 0.1 mL of 1% phenolic solution in 95% ethanol/water. Stepwise, 0.375 mL of 1% NaClO in alkaline sodium citrate solution and 0.5 mL of 0.5% $Na[Fe(CN)_5NO]$ solution were added. The assayed aliquots were aged overnight before being analyzed on a Xevo LCMS-ESI system. For NMR measurement, 10 mL of the assay was taken out, and its pH was adjusted to 3 by the addition of 0.5 M H_2SO_4. Next, 0.9 mL of the resulting liquid was taken out, and then 0.1 mL of D_2O was added as an internal standard. The ^1H NMR signal of $^{15}NH_4^+$ is split by the nuclear spin of ^{15}N into a doublet (~73 Hz) in the region near 7.0 ppm. A calibration curve (Figure S7) was obtained for the integration of this signal as a function of concentration with standard solutions made up from $^{15}NH_4^+$, and pH was adjusted to 3 by the addition of 0.5 M H_2SO_4. A known quantity of d^6-DMSO was added as an internal standard. All experiments were undertaken with water suppression.

Photocatalytic activity tests with a solar furnace and a fixed-bed reactor

The photocatalytic ammonia synthesis was also investigated in a solar furnace, in which light was the only energy source and no electrical heating device was engaged. The conditions were the same as those for the typical photocatalytic ammonia synthesis activity test previously mentioned. However, the light source was generated by a four-mirror floating-zone light furnace (operated at 60.9 V, 15.08 A, and 918 W) from Crystal Systems equipped with four halogen lamps to mimic a solar concentrator: the concentrated light was applied through the quartz windows to heat the autoclave reactor to 270°C at the saturated equilibrium pressure of water and at the same time the irradiated photocatalyst. After a 2 h reaction, the autoclave was allowed to cool down naturally, and the amounts of hydrogen and oxygen were measured by a gas chromatograph equipped with thermal conductivity detectors. A continuous-flow mode reactor with a home-made light illumination system was also used to evaluate the photocatalysis over Fe-sMoS_2. The light illumination area was 14.13 mm^2. N_2 (10 mL min^{-1}) first passed through Milli-Q water before flowing into the reactor. The outlet gas was first passed through a H_2SO_4 trap and then flowed into an on-line gas chromatograph to detect H_2. The temperature was raised to 270°C.

SUPPLEMENTAL INFORMATION

Supplemental information can be found online at https://doi.org/10.1016/j.checat.2021.03.002.

ACKNOWLEDGMENTS

The support of this project from the EPSRC in the UK (DGE 102000) is gratefully acknowledged. The authors wish to thank AIST in Japan and NSRRC in Taiwan for accessing STEM and XAS facilities. J.Z. and P.Z. also acknowledge I15-1 at the Diamond Light Source in Oxford, UK, for XPDF. We appreciate the support of K.A. Vincent for the *in situ* IR measurement. L.L. also acknowledges the use of the computing facilities of the Wuhan University of Science and Technology in the completion of the theoretical part of this work.

AUTHOR CONTRIBUTIONS

J.Z. prepared, characterized, and tested the catalysts. L.L. performed the DFT calculations. G.L. helped in optimizing some of the structures. D.P., Y.L., and J.Z. performed the solar furnace experiments. I.J.M. and J.Z. conducted the *in situ* ATR-IR and ammonia detection. R.K., K.S., and P.-L.H. did the STEM, EELS, and their analysis. J.Z. and P.Z. analyzed the XPDF. L.B. and J.S. conducted the fluorescence spectroscopy and TAS. T.-S.W., Y.-L.S., J.Z., K.L., and S.W. performed the XAS experiments and conducted the analysis. Y.L. and R.A.T. collected and analyzed the TRPL data. J.Z. and S.C.E.T. wrote the paper. S.C.E.T. supervised the overall project.

DECLARATION OF INTERESTS

The authors declare no competing interests.

Received: January 25, 2021
Revised: February 21, 2021
Accepted: March 3, 2021
Published: April 2, 2021

REFERENCES

1. Avenier, P., Taoufik, M., Lesage, A., Solans-Monfort, X., Baudouin, A., de Mallmann, A., Veyre, L., Basset, J.M., Eisenstein, O., Emsley, L., et al. (2007). Dinitrogen dissociation on an isolated surface tantalum atom. Science *317*, 1056–1060.
2. Liu, J., Kelley, M.S., Wu, W., Banerjee, A., Douvalis, A.P., Wu, J., Zhang, Y., Schatz, G.C., and Kanatzidis, M.G. (2016). Nitrogenase-mimic iron-containing chalcogels for photochemical reduction of dinitrogen to ammonia. Proc. Natl. Acad. Sci. *113*, 5530–5535.
3. Gilbert, P., and Thornley, P. (2010). Energy and carbon balance of ammonia production from biomass gasification (Birmingham, UK: Proceedings of the 2010 Bioten Conference on Biomass, Bioenergy and Biofuels).
4. Malmali, M., Wei, Y., McCormick, A., and Cussler, E.L. (2016). Ammonia synthesis at reduced pressure via reactive separation. Ind. Eng. Chem. Res. *55*, 8922–8932.
5. Ye, L., Nayak-Luke, R., Bañares-Alcántara, R., and Tsang, E. (2017). Reaction: "Green" ammonia production. Chem *3*, 712–714.
6. Hoffman, B.M., Lukoyanov, D., Yang, Z.Y., Dean, D.R., and Seefeldt, L.C. (2014). Mechanism of nitrogen fixation by nitrogenase: the next stage. Chem. Rev. *114*, 4041–4062.
7. Gray, H.B., and Ellis, W.R., Jr. (1994). Electron transfer. In Bioinorganic Chemistry, I. Bertini, H.B. Gray, S.G. Lippard, and J.S. Valentine, eds. (University Science Books), pp. 315–363.
8. Rod, T.H., Logadottir, A., and Nørskov, J.K. (2000). Ammonia synthesis at low temperatures. J. Chem. Phys. *112*, 5343–5347.
9. Hoffman, B.M., Lukoyanov, D., Dean, D.R., and Seefeldt, L.C. (2013). Nitrogenase: a draft mechanism. Acc. Chem. Res. *46*, 587–595.
10. Rittle, J., McCrory, C.C.L., and Peters, J.C.A. (2014). 106-fold enhancement in N_2-binding affinity of an $Fe_2(\mu\text{-}H)_2$ core upon reduction to a mixed-valence $Fe^{II}Fe^{I}$ state. J. Am. Chem. Soc. *136*, 13853–13862.
11. Rittle, J., and Peters, J.C. (2016). An Fe-N_2 complex that generates hydrazine and ammonia via Fe N=NH_2: demonstrating a hybrid distal-to-alternating pathway for N_2 reduction. J. Am. Chem. Soc. *138*, 4243–4248.
12. Buscagan, T.M., Oyala, P.H., and Peters, J.C. (2017). N_2-to-NH_3 conversion by a triphos-iron catalyst and enhanced turnover under photolysis. Angew. Chem. Int. Ed. *56*, 6921–6926.
13. Li, Y., Li, Y., Wang, B., Luo, Y., Yang, D., Tong, P., Zhao, J., Luo, L., Zhou, Y., Chen, S., et al. (2013). Ammonia formation by a thiolate-bridged diiron amide complex as a nitrogenase mimic. Nat. Chem *5*, 320–326.
14. Broda, H., and Tuczek, F. (2014). Catalytic ammonia synthesis in homogeneous solution—biomimetic at last? Angew. Chem. Int. Ed. *53*, 632–634.
15. Eda, G., Fujita, T., Yamaguchi, H., Voiry, D., Chen, M., and Chhowalla, M. (2012). Coherent atomic and electronic heterostructures of single-layer MoS_2. ACS Nano *6*, 7311–7317.
16. Moniz, S.J., Shevlin, S.A., Martin, D.J., Guo, Z.X., and Tang, J. (2015). Visible-light driven heterojunction photocatalysts for water splitting—a critical review. Energy Environ. Sci. *8*, 731–759.
17. Wang, J., Tafen de, N., Lewis, J.P., Hong, Z., Manivannan, A., Zhi, M., Li, M., and Wu, N. (2009). Origin of photocatalytic activity of nitrogen-doped TiO_2 nanobelts. J. Am. Chem. Soc. *131*, 12290–12297.
18. Li, Y., Peng, Y.K., Hu, L., Zheng, J., Prabhakaran, D., Wu, S., Puchtler, T.J., Li, M., Wong, K.Y., Taylor, R.A., and Tsang, S.C.E. (2019). Photocatalytic water splitting by N-TiO_2 on MgO (111) with exceptional quantum efficiencies at elevated temperatures. Nat. Commun *10*, 4421.
19. Guo, L., Robertson, A.W., Li, M.M., Kuo, W.C.H., Darby, M.T., Muhieddine, M.H., Lin, Y.C., Suenaga, K., Stamatakis, M., Warner, J.H., and Tsang, S.C.E. (2013). MoS_2 monolayer catalyst doped with isolated Co atoms for the hydrodeoxygenation reaction. Nat. Chem *9*, 810–816.
20. Cao, Y., Fatemi, V., Fang, S., Watanabe, K., Taniguchi, T., Kaxiaras, E., and Jarillo-Herrero, P. (2018). Unconventional superconductivity in magic-angle graphene superlattices. Nature *556*, 43.
21. Hachtel, J.A., Yu, S., Lupini, A.R., Pantelides, S.T., Gich, M., Laromaine, A., and Roig, A. (2016). Gold nanotriangles decorated with superparamagnetic iron oxide nanoparticles: a compositional and microstructural study. Farad. Diss. *191*, 215–227.
22. Fei, H., Dong, J., Arellano-Jiménez, M.J., Ye, G., Dong Kim, N., Samuel, E.L., Peng, Z., Zhu, Z., Qin, F., Bao, J., et al. (2015). Atomic cobalt on nitrogen-doped graphene for hydrogen generation. Nat. Commun. *6*, 8668.
23. Bjornsson, R., Neese, F., Schrock, R.R., Einsle, O., and DeBeer, S. (2015). The discovery of Mo (III) in FeMoco: reuniting enzyme and model chemistry. J. Bio. Ino. Chem. *20*, 447–460.
24. van der Ham, C.J.M., Koper, M.T.M., and Hetterscheid, D.G.H. (2014). Challenges in reduction of dinitrogen by proton and electron transfer. Chem. Soc. Rev. *43*, 5183–5191.
25. Reddy, D.A., Park, H., Hong, S., Kumar, P., and Kim, T.K. (2017). Hydrazine-assisted formation of ultrathin MoS_2 nanosheets for enhancing their co-catalytic activity in photocatalytic hydrogen evolution. J. Mater. Chem. A. *5*, 6981–6991.
26. Shi, H., Yan, R., Bertolazzi, S., Brivio, J., Gao, B., Kis, A., Jena, D., Xing, H.G., and Huang, L. (2013). Exciton dynamics in suspended monolayer and few-layer MoS_2 2D crystals. ACS Nano *7*, 1072–1080.

27. Wu, Z., Li, L., Wang, L., Liu, Y., Sun, W., Li, W., and Li, G. (2013). MoS_2 nanosheets: a designed structure with high active site density for the hydrogen evolution reaction. ACS Catal. *3*, 2101–2107.

28. Jing, L., Qu, Y., Wang, B., Li, S., Jiang, B., Yang, L., Fu, W., Fu, H., and Sun, J. (2006). Review of photoluminescence performance of nano-sized semiconductor materials and its relationships with photocatalytic activity. Sol. Energy Mater. Sol. Cells *90*, 1773–1787.

29. Yao, Y., Zhu, S., Wang, H., Li, H., and Shao, M. (2018). A spectroscopic study on the nitrogen electrochemical reduction reaction on gold and platinum surfaces. J. Am. Chem. Soc. *140*, 1496–1501.

30. Watt, G.W., and Chirsp, J.D. (1952). Spectrophotometric method for determination of hydrazine. Anal. Chem. *24*, 2006–2008.

31. Lin, C.H., Lin, H.S., Huang, C.C., Su, S.K., Lin, S.D., Sun, K.W., Lee, C.P., Liu, Y.K., Yang, M.D., and Shen, J.L. (2009). Temperature dependence of time-resolved photoluminescence spectroscopy in InAs/GaAs quantum ring. Appl. Phys. Lett. *94*, 183101.

32. Okamoto, K., Niki, I., Scherer, A., Narukawa, Y., Mukai, T., and Kawakami, Y. (2005). Surface plasmon enhanced spontaneous emission rate of InGaN/GaN quantum wells probed by time-resolved photoluminescence spectroscopy. Appl. Phys. Lett. *87*, 071102.

33. Smith, M., Chen, G.D., Lin, J.Y., Jiang, H.X., Asif Khan, M., and Chen, Q. (1996). Time-resolved photoluminescence studies of InGaN epilayers. Appl. Phys. Lett. *69*, 2837–2839.

34. Hisatomi, T., and Domen, K. (2019). Reaction systems for solar hydrogen production via water splitting with particulate semiconductor photocatalysts. Nat. Catal. *2*, 387–399.

35. Takata, T., and Domen, K. (2019). Particulate photocatalysts for water splitting: recent advances and future prospects. ACS Energy Lett *4*, 542–549.

36. Pinaud, B.A., Benck, J.D., Seitz, L.C., Forman, A.J., Chen, Z., Deutsch, T.G., James, B.D., Baum, K.N., Baum, G.N., Ardo, S., et al. (2013). Technical and economic feasibility of centralized facilities for solar hydrogen production via photocatalysis and photoelectrochemistry. Energy Environ. Sci. *6*, 1983–2002.

37. Sieling, K., Günther-Borstel, O., and Hanus, H. (1997). Effect of slurry application and mineral nitrogen fertilization on N leaching in different crop combinations. J. Agr. Sci. *128*, 79–86.

38. Funke, H., Chukalina, M., and Scheinost, A.C. (2007). A new FEFF-based wavelet for EXAFS data analysis. J. Synch. Rad. *14*, 426–432.

39. Gangwar, J., Gupta, B.K., Kumar, P., Tripathi, S.K., and Srivastava, A.K. (2014). Time-resolved and photoluminescence spectroscopy of θ-Al_2O_3 nanowires for promising fast optical sensor applications. Dalton Trans. *43*, 17034–17043.

40. Li, M.M.J., Mills, P., Fairclough, S.M., Robertson, A., Peng, Y.K., Warner, J., Nie, C., Flahaut, E., and Tsang, S.C.E. (2016). Importance of the structural integrity of a carbon conjugated mediator for photocatalytic hydrogen generation from water over a CdS-carbon nanotube-MoS_2 composite. Chem. Commun. *52*, 13596–13599.

41. Hidalgo, R., Ash, P.A., Healy, A.J., and Vincent, K.A. (2015). Infrared spectroscopy during electrocatalytic turnover reveals the Ni-L active site state during H_2 oxidation by a NiFe hydrogenase. Angew. Chem. Int. Ed. *54*, 7110–7113.

42. Kresse, G., and Hafner, J. (1993). Ab initio molecular dynamics for liquid metals. Phys. Rev. B *47*, 558–561.

43. Perdew, J.P., Burke, K., and Ernzerhof, M. (1996). Generalized gradient approximation made simple. Phys. Rev. Lett. *77*, 3865–3868.

44. Blochl, P.E. (1994). Projector augmented-wave method. Phys. Rev. B: Condens. Matter Mater. Phys. *50*, 17953–17979.

45. Monkhorst, H.J., and Pack, J.D. (1976). Special points for Brillouin-zone integrations. Phys. Rev. B: Solid State *13*, 5188–5192.

46. Andersen, S.Z., Čolić, V., Yang, S., Schwalbe, J.A., Nielander, A.C., McEnaney, J.M., Enemark-Rasmussen, K., Baker, J.G., Singh, A.R., Rohr, B.A., et al. (2019). A rigorous electrochemical ammonia synthesis protocol with quantitative isotope measurements. Nature *570*, 504–508.

47. Choi, J., Du, H.L., Nguyen, C.K., Suryanto, B.H., Simonov, A.N., and MacFarlane, D.R. (2020). Electroreduction of nitrates, nitrites, and gaseous nitrogen oxides: a potential source of ammonia in dinitrogen reduction studies. ACS Energy Lett *5*, 2095–2097.